The Astrophysical Journal, 980:70 (16pp), 2025 February 10 https://doi.org/10.3847/1538-4357/ada699

Differentiating the Acceleration Mechanisms in the Slow and Alfvénic Slow Solar Wind

Yeimy J. Rivera[1], Samuel T. Badman[1], J. L. Verniero[2], Tania Varesano[3,4], Michael L. Stevens[1], Julia E. Stawarz[5], Katharine K. Reeves[1], Jim M. Raines[6], John C. Raymond[1], Christopher J. Owen[7], Stefano A. Livi[6,8], Susan T. Lepri[6], Enrico Landi[6], Jasper. S. Halekas[9], Tamar Ervin[10,11], Ryan M. Dewey[6], Rossana De Marco[12], Raffaella D'Amicis[12], Jean-Baptiste Dakeyo[13,14], Stuart D. Bale[11,15], and B. L. Alterman[2]

[1] Center for Astrophysics | Harvard & Smithsonian, 60 Garden Street, Cambridge, MA 02138, USA
[2] Heliophysics Laboratory, NASA Goddard Space Flight Center, 8800 Greenbelt Road, Greenbelt, MD 20771, USA
[3] Southwest Research Institute, Boulder, CO 80302, USA
[4] Department of Aerospace Engineering Sciences, University of Colorado Boulder, Boulder, CO 80303, USA
[5] Department of Mathematics, Physics, and Electrical Engineering, Northumbria University, Newcastle upon Tyne, UK
[6] Department of Climate & Space Sciences & Engineering, University of Michigan, 2455 Hayward Street, Ann Arbor, MI 48109-2143, USA
[7] Mullard Space Science Laboratory, University College London, Holmbury St. Mary, Dorking, Surrey, RH5 6NT, UK
[8] Southwest Research Institute, San Antonio, TX 78228, USA
[9] Department of Physics and Astronomy, University of Iowa, Iowa City, IA 52242, USA
[10] Department of Physics, University of California, Berkeley, Berkeley, CA 94720-7300, USA
[11] Space Sciences Laboratory, University of California, Berkeley, Berkeley, CA 94720-7450, USA
[12] INAF—Institute for Space Astrophysics and Planetology, Rome, Italy
[13] LESIA, Observatoire de Paris, Université PSL, CNRS, Sorbonne Université, Université de Paris, 5 place Jules Janssen, 92195 Meudon, France
[14] IRAP, Observatoire Midi-Pyrénées, Université Toulouse III—Paul Sabatier, CNRS, 9 Avenue du Colonel Roche, 31400 Toulouse, France
[15] Physics Department, University of California, Berkeley, Berkeley, CA 94720-7300, USA
Received 2024 November 6; revised 2025 January 3; accepted 2025 January 3; published 2025 February 5

Abstract

In the corona, plasma is accelerated to hundreds of kilometers per second and heated to temperatures hundreds of times hotter than the Sun's surface before it escapes to form the solar wind. Decades of space-based experiments have shown that the energization process does not stop after it escapes. Instead, the solar wind continues to accelerate, and it cools far more slowly than a freely expanding adiabatic gas. Recent work suggests that fast solar wind requires additional momentum beyond what can be provided by the observed thermal pressure gradients alone, whereas it is sufficient for the slowest wind. The additional acceleration for fast wind can be provided through an Alfvén wave pressure gradient. Beyond this fast/slow categorization, however, a subset of slow solar wind exhibits high Alfvénicity that suggests that Alfvén waves could play a larger role in its acceleration compared to conventional slow wind outflows. Through a well-timed conjunction between Solar Orbiter and Parker Solar Probe (PSP), we trace the energetics of slow wind to compare with a neighboring Alfvénic slow solar wind stream. An analysis that integrates remote and heliospheric properties and modeling of the two distinct solar wind streams finds that Alfvénic slow solar wind behaves like fast wind, where a wave pressure gradient is required to reconcile its full acceleration, while non-Alfvénic slow wind can be driven by its nonadiabatic electron and proton thermal pressure gradients. Derived coronal conditions of the source region indicate good model compatibility, but extended coronal observations are required to effectively trace solar wind energetics below PSP's orbit.

Unified Astronomy Thesaurus concepts: Solar wind (1534); Slow solar wind (1873); Alfvén waves (23); Chemical abundances (224)

1. Introduction

With the launch of Parker Solar Probe (PSP; N. J. Fox et al. 2016) in 2018, the heliospheric community has been able to observe solar wind at distances closer than ever before, extending our view nearer to where the solar wind is actively heated and accelerated. One of the most notable discoveries from PSP was the near-ubiquitous appearance of high-amplitude magnetic field reversals, or magnetic switchbacks, near perihelion passes (S. D. Bale et al. 2019; J. C. Kasper et al. 2019). The switchbacks are Alfvénic in nature (J. W. Belcher & L. J. Leverett 1971), characterized by a rapid change in the magnetic field direction and correlated velocity and magnetic field fluctuations with near-constant magnetic field magnitude. Switchbacks are typically observed to cluster together in coherent patches consisting of many individual velocity and magnetic field spikes with sharp discontinuities at their boundaries (T. S. Horbury et al. 2020). The spatial scales of patches are of the scale of supergranulation at the Sun and contain compositional signatures suggesting that they are linked to the boundaries of coronal holes (S. D. Bale et al. 2021; N. Fargette et al. 2021; Y. J. Rivera et al. 2024a). From a statistical analysis coupling PSP, Helios, and Ulysses data, it is found that switchback occurrence with radial distance depends on their duration and size. Shorter-duration switchbacks decrease in cumulative counts per kilometer, while larger-scale switchbacks increase, suggesting a dynamic radial evolution (A. Tenerani et al. 2021; V. K. Jagarlamudi et al. 2023). Given the gradual restructuring of switchbacks with increasing heliocentric distance, their decay is an attractive process for explaining the additional heating and acceleration experienced by the solar wind at the inner heliosphere.

Until recently, a comprehensive assessment of the energy sources and physical mechanisms driving outflow dynamics

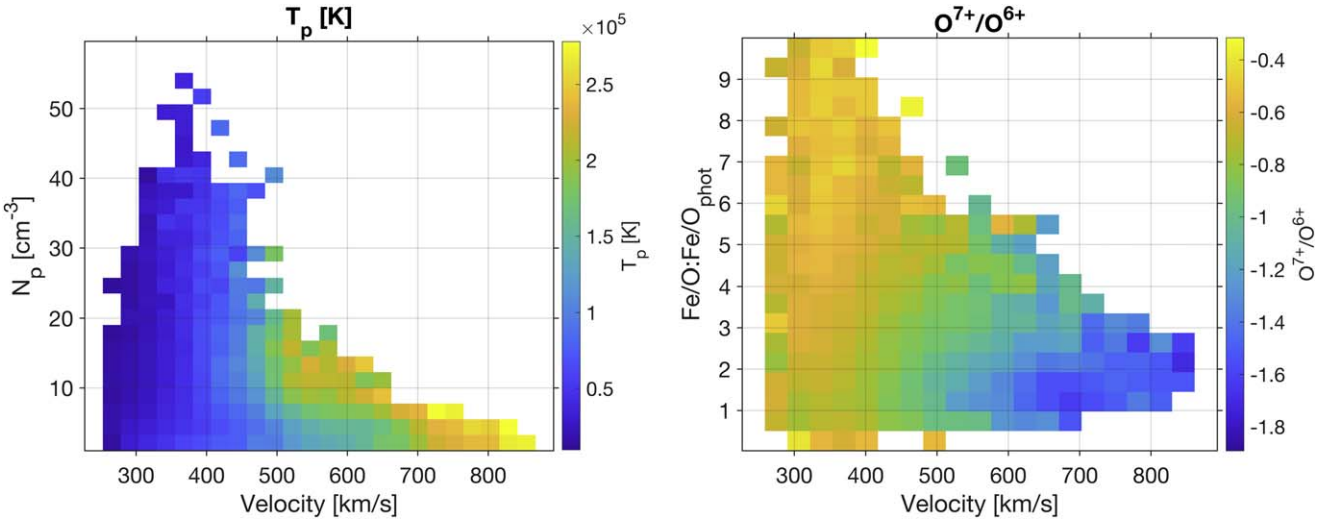

Figure 1. 2D histograms showing the distribution of proton density across wind speed (left), where the color indicates the average proton temperature, and Fe/O:Fe/O_{phot}, the ratio of elemental Fe to O normalized to its photospheric abundances across wind speed (right), where the color indicates the O^{7+}/O^{6+} ion ratio.

has only been quantified on a statistical basis. For example, J. S. Halekas et al. (2023) examine the energy budget of the solar wind to quantify the role of the proton pressure, ambipolar electric potential, and wave energy in the acceleration of different speed streams. Through statistical observations from PSP across 13.3–100 $R_{\odot}$, J. S. Halekas et al. (2023) find that the contribution of wave energy flux becomes increasingly important to explain the acceleration of the fast speed wind. Conversely, the acceleration of the slower speed wind can be captured entirely through the electron thermal gradient (or, equivalently, the ambipolar potential; J. S. Halekas et al. 2022). This result strongly suggests that the energy content from Alfvén waves is a critical energy component required to explain the extended heating and acceleration of coronal hole wind. Recent work by Y. J. Rivera et al. (2024b) confirmed that large-amplitude Alfvén waves assembled in switchback patches contained the necessary energy to explain the heating and acceleration experienced by a moderately fast wind stream across the inner heliosphere. However, such an analysis has not been carried out for the energetics of the slow speed wind beyond the corona. D. Telloni et al. (2023a) find the energy partitioning of a slow wind stream (with a predicted 450 km s^{-1} asymptotic speed) in the corona, below <13 $R_{\odot}$, indicating that the acceleration is driven by the wave energy flux and electric potential. Our analysis will track the flow of slow wind beyond the corona to quantify the energetics driving its evolution just beyond the Alfvén surface, a location that marks where the solar wind increases above the local Alfvén speed.

In particular, the slow speed wind is more variable compared to the fast wind (L. Abbo et al. 2016), often encompassing properties usually observed in the faster speed wind, e.g., elemental composition (S. T. Lepri et al. 2013; M. Stakhiv et al. 2015), coronal temperature as indicated by charge states (F. Xu & J. E. Borovsky 2015; Y. M. Wang 2016), variable mass flux, variation in its Alfvénicity as indicated by its cross-helicity (R. D'Amicis & R. Bruno 2015; D. Perrone et al. 2020; D. Perrone et al. 2022), and helium abundance (K. W. Ogilvie & J. Hirshberg 1974; M. R. Aellig et al. 2001; J. C. Kasper et al. 2007, 2012; B. L. Alterman & J. C. Kasper 2019; B. L. Alterman et al. 2021), which indicate diverse coronal sources (D. Baker et al. 2023; B. J. Lynch et al. 2023; T. Ervin et al. 2024a, 2024a). The variability of slow solar wind properties is characterized by 2D histograms in Figure 1 of the indicated properties from observations taken by the Advanced Composition Explorer (ACE; E. C. Stone et al. 1998) collected between 1998 and 2011. The figure shows the relationship between the different parameters and the variability of the slow wind as compared to the fast speed wind across solar cycle 23 within all parameters. Of particular interest for the present study, recent work has subcategorized the slow speed wind as Alfvénic or non-Alfvénic through its cross-helicity character, suggesting that the wave energy can vary across solar wind of similar speed (R. D'Amicis & R. Bruno 2015; R. D'Amicis et al. 2019).

To effectively investigate the role of the thermal and wave energy fluxes and their associated thermal pressure and Alfvén wave pressure gradient in connection with the Alfvénic and non-Alfvénic slow solar wind dynamics, it is necessary to examine their radial evolution within the stream. Such a connection can only be accomplished during conjunctions between the different spacecraft that align to intersect the same solar wind stream at different stages of its evolution. These kinds of coordinated observations enable the direct assessment of energy transfer over this region, connecting the dynamics and heating to the dissipation of the energy content of the Alfvén waves necessary for the present study (M. Velli et al. 2020).

To capture the slow solar wind evolution, this work examines a spacecraft co-alignment that sampled the same solar wind streams (as supported by several pieces of evidence, including stream mapping and compositional diagnostics) at the sub-Alfvénic periphery to $\sim$0.6 au, where the escaping solar wind is connected to fully formed solar wind. By connecting the solutions from a Parker solar wind model (E. N. Parker 1958, 1960; J.-B. Dakeyo et al. 2022; C. Shi et al. 2022) constrained by measurements at both spacecraft, as well as at the corona through remote observations, large-scale energetics are traced across an expanding flux tube in each stream. We show that the Alfvén waves in the form of switchbacks carry and, ultimately, dissipate energy at the order of magnitude needed to sustain both the temperature gradient and acceleration observed in the Alfvénic slow solar wind stream. This result strongly suggests that, as observed in the

fast solar wind (Y. J. Rivera et al. 2024b), the dissipation of Alfvén wave energy carried by magnetic switchbacks and momentum transferred to the particles continues to power the Alfvénic slow speed wind across the inner heliosphere. For the non-Alfvénic slow solar wind, we find that it is completely accelerated by the proton and electron thermal pressure gradient in the stream with an insignificant contribution from the large-scale wave pressure gradient. Derived temperature and density from remote observations of the Alfvénic slow wind source region show fairly good agreement with modeling results. However, a more rigorous examination of the extended corona, through thoughtful and dedicated multispacecraft coordination, is necessary to trace energetics from the low corona and beyond. We note that details of the Alfvén wave dissipation processes themselves are not examined in this study but are critical to understanding how energy is transferred from larger Alfvénic fluctuations to smaller scales and ultimately dissipated to heat the plasma and partitioned between ions and electrons (e.g., C. A. González et al. 2021; L. Adhikari et al. 2021; N. Sioulas et al. 2022; R. Bandyopadhyay et al. 2023; S. Bourouaine et al. 2024).

The paper is organized as follows: Section 2 discusses the observations, conjunction period, ballistic mapping, and solar wind properties. Section 3 presents the mass, magnetic, and energy flux conservation in the streams. Section 4 presents the source region analysis. Section 5 presents the model implementation and results. Sections 6 and 7 present the discussion and conclusions, respectively.

2. Observations

2.1. Parker Solar Probe and Solar Orbiter Observations

To compute the stream properties and energetics of the slow and Alfvén slow wind, we examine properties of the solar wind in situ during a conjunction between PSP and Solar Orbiter that occurred in 2022 February/March during PSP's 11th perihelion pass.

At PSP, we examine observations from the SPAN-Ai instrument to compute proton and alpha number densities, temperatures, and bulk velocities (R. Livi et al. 2022). SPAN-Ai couples an electrostatic analyzer and time-of-flight (TOF) component to resolve incident angle, mass per charge, and energy per charge of incoming ions. The mass discrimination made possible by the TOF analyzer allows for the identification of separate ion species in the solar wind, mainly the most abundant species—protons and alpha particles. SPAN-Ai provides individual 3D particle distributions of proton and alpha particles, at 1.75 s cadence. Due to obstruction of the instrument by the heat shield and solar panels, portions of velocity space are at times unobservable, with severity varying according to the direction of flow in the spacecraft frame. We discuss the treatment of the SPAN-Ai observations in the following section. We include electron measurements from SPAN-Ae (P. L. Whittlesey et al. 2020). Additionally, the 3D magnetic field components are measured by the fluxgate magnetometer (MAG) on FIELDS at four vectors per cycle to capture the rapid changes in the magnetic field (S. D. Bale et al. 2016).

At Solar Orbiter, measurements of the magnetic field are taken by another fluxgate magnetometer (MAG) at eight vectors per second (T. S. Horbury et al. 2020). Observations of protons, alpha particles, and heavier ions across this period were taken by the Proton-Alpha System (PAS) and Heavy Ion Sensor (HIS) instruments that are part of the Solar Wind Analyzer (SWA) suite (C. J. Owen et al. 2020). The proton and alpha densities, temperatures, and velocities were measured with the PAS instrument with 4 s full-scan 3D particle distributions. Properties of the alpha population were determined from the PAS measurements using a machine learning statistical clustering technique detailed in R. De Marco et al. (2023). Observations of the heavier ions ($Z > 2$) were obtained at a 10-minute resolution using the TOF mass spectrometer HIS (S. Livi et al. 2023).

2.2. Coinciding Remote Sensing Observations

To place a constraint on the modeling results in the low corona, we analyze the source region conditions of the solar wind footpoints. We use the Spectral Imaging of the Coronal Environment (SPICE; SPICE Consortium et al. 2020) instrument aboard Solar Orbiter and Hinode's EUV Imaging Spectrometer (EIS; J. L. Culhane et al. 2007) to derive elemental composition, electron density, and temperature of the coronal hole identified as the solar wind source region for the intervals of interest in this work. SPICE is a high-resolution spectrometer measuring two EUV wavelength bands between 704–790 Å and 973–1049 Å. SPICE observations were taken on 2022 February 23 11:23–10:06 UT with a 60 s exposure and 2″ slit covering a 768″ × 630.″25 region of the Sun. Near-contemporaneous Hinode/EIS observations were taken on 2022 February 23 00:30–01:31 UT in two wavelength ranges from 171–211 Å to 245–291 Å with a 2″ slit across a 260″ × 512″ field of view (FOV) with a 60 s exposure. The Solar Orbiter position was 6° from the Sun–Earth line, where EIS observations were taken. For context, we use the Solar Dynamics Observatory/Atmospheric Imaging Assembly (SDO/AIA; J. R. Lemen et al. 2012) 193 Å image, as well as a full-Sun image (FSI; P. Rochus et al. 2020) in the 174 Å channel from Solar Orbiter. The two rasters overlap in a small region. For the analysis, footpoint mapping of the slow Alfvénic wind covered a portion of the SPICE FOV and an overlapping region of the EIS FOV as discussed in Section 4.

We note that during 2021 December 28–2022 March 1 there was a problem with the Hinode attitude control system related to maintaining a stable roll angle.[16] Therefore, the EIS observations in the present work were taken while the instrument was rotated, causing the FOV to be 93° counterclockwise rotated as well. The pointing information for the raster was adjusted manually where the Fe XII 195.119 Å was lined up with features of the AIA 193 Å channel (where the Fe XII line is dominant), as is typically done. For our purposes, adjustment will not affect the coronal analysis since we are interested in the large-scale conditions of the source region.

2.3. Stream Matching

In PSP Encounter 11, the spacecraft was in close PSP spiral alignment with Solar Orbiter for a period centered on February 25 (T. Ervin et al. 2024a; Y. J. Rivera et al. 2024b, 2024a). This conjunction is illustrated for the solar corotating (Carrington) frame in Figure 2. The top and bottom panels show respectively the streams projected into the heliographic equatorial plane and the trajectories ballistically mapped

[16] https://solarb.mssl.ucl.ac.uk/JSPWiki/Wiki.jsp?page=EISHistory

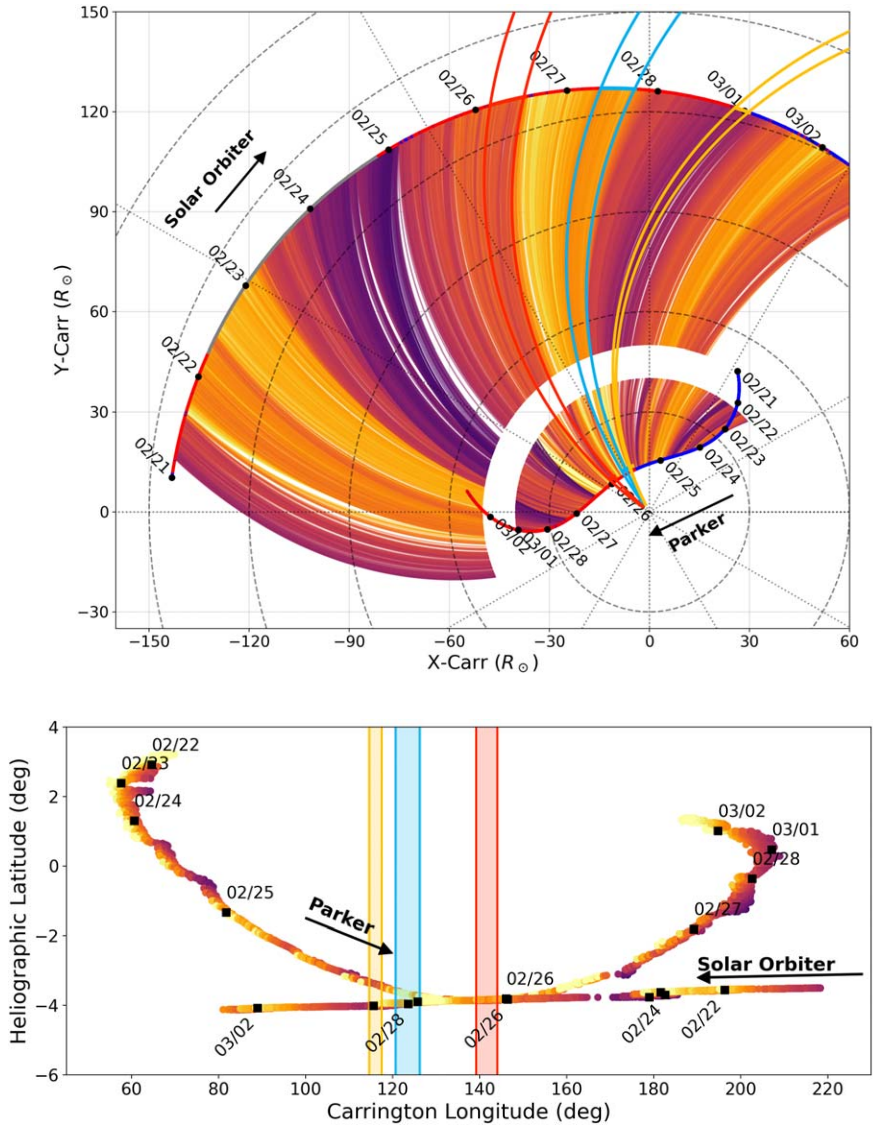

Figure 2. Illustration of the conjunction and ballistic mapping in the Carrington frame. Top: Solar Orbiter's and PSP's trajectories projected into the solar equatorial plane for late 2022 February. Colored PSP spiral field lines illustrate how Solar Orbiter's and PSP's measurements are ballistically propagated inward to the Sun. Bottom: the ballistically mapped heliographic coordinates for PSP and Solar Orbiter at 2.5 $R_\odot$. PSP spirals bounded by the red, blue, and yellow flow lines (top) and vertical lines (bottom) annotate the slow Alfvénic, fast, and slow stream, respectively, which we follow from PSP out to Solar Orbiter, corresponding to the time frames highlighted in the corresponding colors in Figure 3.

(D. Stansby et al. 2019; S. T. Badman et al. 2020) to an altitude of 2.5 $R_\odot$. The ballistic mapping utilizes the heliographic location of the relevant spacecraft and the measured solar wind velocity to define a PSP spiral field line that approximately traces the path of the relevant plasma parcel back to its origin in the outer corona (J. T. Nolte & E. C. Roelof 1973; A. Koukras et al. 2022; A. R. Macneil et al. 2022; J. B. Dakeyo et al. 2024).

In Figure 2, date labels show how PSP and Solar Orbiter move in opposite heliographic directions and cross the same streams in reverse order at different heliocentric distances. The x-axis of the right panel is the ballistically mapped source surface longitude, which is used to identify the time frames of solar wind measured between PSP and Solar Orbiter, cited in this section. A pair of solid curves of constant source surface longitude shown in both panels isolate a slow (yellow), a fast (blue), and an Alfvénic slow (red) wind stream observed in both spacecraft. As seen in the bottom panel, this occurs when PSP and Solar Orbiter are also nearly coincident in latitude over an extended range of longitude, which makes this conjunction unique in the mission so far, as we are probing pure radial evolution of multiple streams rather than needing to disentangle radial and latitudinal effects simultaneously.

2.4. Solar Wind Properties

Once a connection was established, we identify the slow and Alfvénic slow solar wind periods by their asymptotic speed at Solar Orbiter and their Alfvénicity as characterized by the normalized cross-helicity at PSP, where this signature is most pristine (W. H. Matthaeus & M. L. Goldstein 1982; R. Bruno & V. Carbone 2013). The solar wind properties from this study corresponding to the portion of the streams, backmapped in Figure 2, are shown in Figure 3 and summarized in Tables 1 and 2. The figure shows the properties of the solar wind at PSP (left column) and Solar Orbiter (right column) in time. We note that the Solar Orbiter data are plotted in reverse time such that the streams appear left to right. Panel (a) shows the magnetic

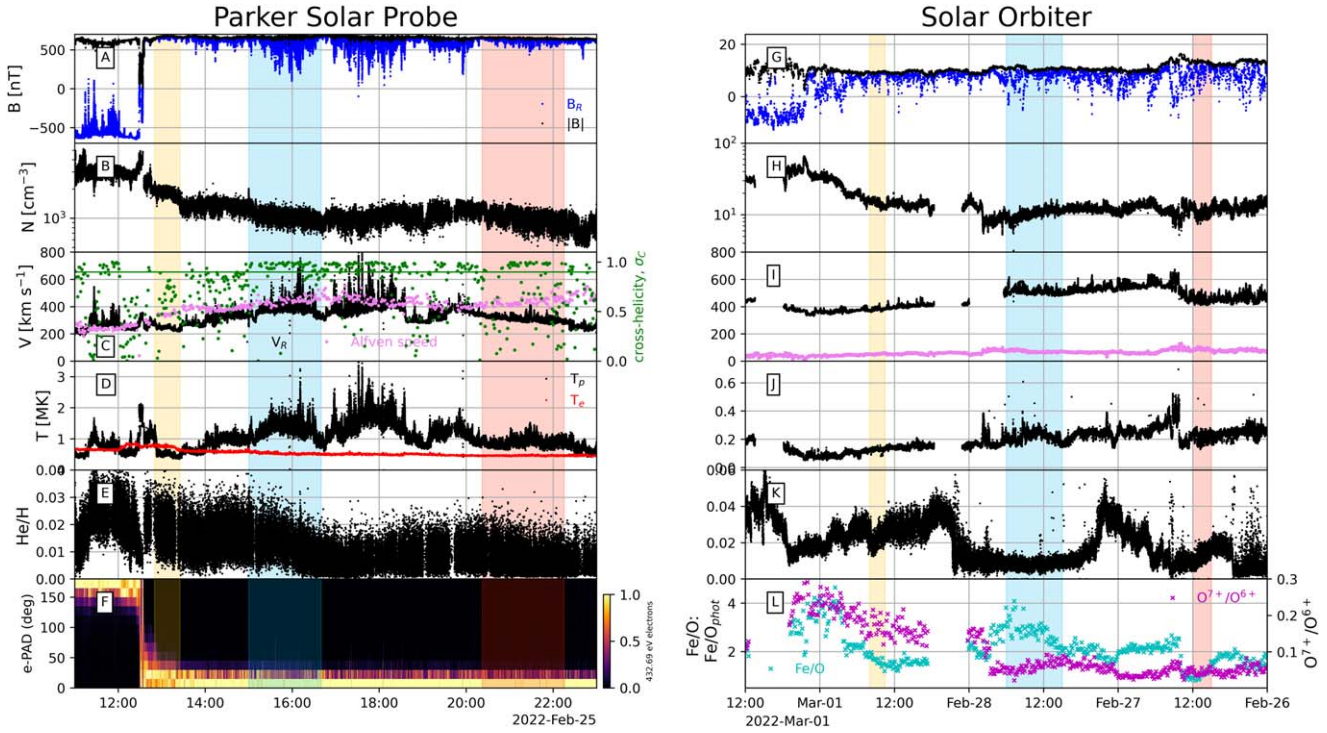

Figure 3. Stackplot showing the solar wind properties at PSP (left) and Solar Orbiter (right), where Solar Orbiter is plotted in reversed time. The shaded region corresponds to the periods of interest. Top to bottom, the first five rows are as follows: (a/g) radial magnetic field component and magnitude; (b/h) proton density; (c/i) proton bulk speed, Alfvén speed, and cross-helicity (only for PSP), where the horizontal green line indicates a value of 0.9; (d/j) isotropic proton and electron (only for PSP) temperature; (f/k) the helium abundance as the He/H number density ratio. Panel (f) is the electron PAD at 432.69 eV. Panel (l) shows the Fe/O:Fe/O$_{\rm phot}$ and O^{7+}/O^{6+} ratio.

Table 1
Characteristic PSP and Solar Orbiter Properties for the Slow Wind Averaged within the Yellow Regions of Figure 3

Properties of Slow Wind	PSP (13.35 $R_\odot$)	Solar Orbiter (125 $R_\odot$)
n_p (cm^{-3})	1712 ± 244	14.8 ± 2.4
v_p (km s^{-1})	251 ± 16	381 ± 10
T_p (MK)	0.6 ± 0.3	0.12 ± 0.1
$V_{\rm A}$ (km s^{-1})	351 ± 22	53 ± 13
B_r (nT)	658 ± 11	8 ± 2
$\lvert B\rvert$ (nT)	667 ± 12	9 ± 0.3
n_α/n_p	0.02 ± 0.005	0.02 ± 0.004
v_α (km s^{-1})	336 ± 36	449 ± 6
T_α (MK)	4.6 ± 2.6	0.65 ± 0.07
T_e (MK)	0.75 ± 0.01	0.27 ± 0.01[a]
δB (nT)	90 ± 46	5.3 ± 2.6

Note.
[a] In lieu of a direct measured constraint, we estimate $T_e|_{\rm SolarOrbiter}$ using $T_e|_{\rm PSP}$ and the statistical electron polytropic index derived by J.-B. Dakeyo et al. (2022) for their solar wind family C.

Table 2
Characteristic PSP and Solar Orbiter Properties for the Alfvénic Slow Wind Averaged within the Red Regions of Figure 3

Properties Alfvénic Slow Wind	PSP (13.7 $R_\odot$)	Solar Orbiter (130.6 $R_\odot$)
n_p (cm^{-3})	1043 ± 211	11 ± 2.8
v_p (km s^{-1})	311 ± 22	451 ± 21
T_p (MK)	0.9 ± 0.12	0.22 ± 0.03
$V_{\rm A}$ (km s^{-1})	439 ± 15	88 ± 7
B_r (nT)	631 ± 21	9.4 ± 3
$\lvert B\rvert$ (nT)	650 ± 7	13.3 ± 0.34
n_α/n_p	0.01 ± 0.005	0.016 ± 0.007
v_α (km s^{-1})	434 ± 53	537 ± 14
T_α (MK)	6.6 ± 2.4	1.1 ± 0.15
T_e (MK)	0.47 ± 0.01	0.17 ± 0.01[a]
δB (nT)	140 ± 71	13 ± 4.6

Note.
[a] In lieu of a direct measured constraint, we estimate $T_e|_{\rm SolarOrbiter}$ using $T_e|_{\rm PSP}$ and the statistical electron polytropic index derived by J.-B. Dakeyo et al. (2022) for their solar wind family D.

field magnitude and radial component. Panel (b) shows the proton density. Panel (c) shows the radial speed (black), Alfvén speed (pink) as $V_{\rm A} = |\boldsymbol{B}|/\sqrt{\mu_0 m_p n_p}$, and normalized cross-helicity (green), along with a green line noting the 0.9 threshold. Panel (d) shows the proton (black) and electron (red) temperature. Panel (e) shows the helium abundance as

He/H. Panel (f) shows the column-normalized electron pitch-angle distribution (e-PAD) of suprathermal electrons across $0^\circ-180^\circ$ in the energy range of 432.69 eV. Panels (g), (h), (j), and (k) are the same properties at Solar Orbiter. In panel (i) we include the proton speed and Alfvén speed, and panel (l) shows the heavy ion composition of the solar wind, showing the Fe^{6-20+}/O^{5-8+} normalized to $Fe/O_{phot} \sim 2.5$ and $\sim$1, respectively, using a photospheric elemental abundance of $Fe/O_{phot} = 0.059$ (M. Asplund et al. 2021). We also plot the O^{7+}/O^{6+} ion ratio.

We compute the cross-helicity as $\sigma_C = 2\delta\boldsymbol{v}\cdot\delta\boldsymbol{b}/(\delta\boldsymbol{v}^2+\delta\boldsymbol{b}^2)$, where the $\delta\boldsymbol{b} = \delta\boldsymbol{B}/|\boldsymbol{B}|\cdot V_A$ are in Alfvén units (A. Barnes & J. V. Hollweg 1974; W. H. Matthaeus & M. L. Goldstein 1982; D. A. Roberts et al. 1987). Here δB is computed as the magnetic field deviation from the mean field, with $\delta\boldsymbol{B} = \boldsymbol{B} - \langle\boldsymbol{B}\rangle_t$, where $\langle\boldsymbol{B}\rangle_t$ is time averaged over 10-minute intervals, t, at PSP and Solar Orbiter on the order of typical Alfvénic fluctuations (C. Y. Tu & E. Marsch 1995), and δv is computed in the same manner. The cross-helicity can range between -1 and 1, where a value near ±1 indicates strong correlation/anticorrelation between the magnetic and velocity fluctuations when the stream is Alfvénic (S. Perri & A. Balogh 2010; R. D'Amicis et al. 2019).

We examine a specific portion of the slow and Alfvénic slow solar wind highlighted in yellow and red, respectively, in the figure. PSP measured the slow speed stream (yellow) with a relatively low cross-helicity (panel (c)) between 12:50 and 13:30 UT on 2022 February 25, while measurements from Solar Orbiter of the same stream took place at 13:30–16:00 UT on 2022 February 28 with a measured speed of 381 km s^{-1} (panel (i)). For the Alfvénic wind (red), PSP sampled the stream at 15:00–17:00UT on 2022 February 25 with a high cross-helicity (panel (c)), and Solar Orbiter sampled it at 9:00–12:00 UT on 2022 February 26 with a speed of 451 km s^{-1} (panel (i)). We also include the fast wind stream examined in Y. J. Rivera et al. (2024b) for comparison. The slow stream is immediately adjacent to a heliospheric current sheet (HCS) crossing measured by both spacecraft as indicated by the change in polarity (panel (a)) and electron PAD direction (panel (f)). The slow Alfvénic stream is adjacent to several faster and hotter streams seen in both spacecraft. We note that this slow stream measured by PSP begins with a transition from a large proton beam, exemplified by the large temperature increase in panel (d), presumably from reconnection within the HCS as described in T. D. Phan et al. (2022).

The periods in the shaded regions of interest are characterized by a number of clear correspondences between the PSP and Solar Orbiter in situ data. The backmapped streams at both spacecraft match in positive field polarities (panels (a) and (g)) and contain persistent $A_{He} \sim$ %2, or He/H $\times$ 100, and $A_{He} \sim$ %1 for the slow and Alfvénic slow solar wind shown in panels (e) and (k), respectively.

Additionally, we measure the Fe/O first ionization potential (FIP) bias and O^{7+}/O^{6+} in panel (l), which exhibit some variability across the distinct streams. The mean Fe/O FIP bias for the slow, fast, and Alfvénic slow wind stream is 1.63 ± 0.19, 2.3 ± 0.23, and 1.09 ± 0.18, respectively. The variation in the elemental composition of the solar wind suggests distinct sources at the Sun as discussed in Section 4 in connection with remote observations. The ion ratios are 0.17 ± 0.03, 0.06 ± 0.02, and 0.05 ± 0.01, respectively. The ion ratio is a proxy for the electron temperature at the corona, where a higher ratio indicates a hotter source electron temperature. Solar wind around the HCS and in the slowest speed wind is generally more highly ionized compared to fast speed wind, in line with the present observations (S. T. Lepri et al. 2013; F. Xu & J. E. Borovsky 2015).

The chosen source surface longitude ranges and associated time frames yield mass and magnetic flux conservation between the spacecraft, as discussed in Section 3.2. We note that the Alfvénic slow stream (red) contains a relatively lower amplitude switchback patch in the PSP data as compared to the fast wind (blue), which are nearly at the same heliocentric distance. While both streams are sub-Alfvénic as shown in panel (c), the Alfvénic slow wind shows a lower Mach number, $V_{SW}/V_A \sim 0.71$, compared to the fast wind case ($\sim$0.89), which has been connected to larger deflection angles in the magnetic field that may be connected to their lower B_R amplitude (Y. D. Liu et al. 2023). The switchback patch is identified as having correlated, large-amplitude, B_r and v_R fluctuations while maintaining near-constant magnetic field magnitude and persistent electron strahl direction, as shown in panels (a), (c), and (f), respectively. Both B_R and v_R range in amplitude at PSP (between different patches) while appearing overall less coherent in the Solar Orbiter observations.

The fast wind and Alfvénic slow solar wind related to switchback patches occur at markedly different speeds. At PSP, the fast wind stream has an average bulk speed of 386 km s^{-1}, compared to a speed of 512 km s^{-1} at Solar Orbiter. For the Alfvénic slow wind, the mean speed at PSP is 311 km s^{-1}, with acceleration to 451 km s^{-1} at Solar Orbiter. In both cases, the solar wind undergoes significant acceleration between the spacecraft $\sim$13.3–130 $R_\odot$, while also suggesting that the acceleration experienced by individual solar wind streams is related to the amplitude of the switchbacks near the Sun.

3. Conservation Equations in the Flux Tube

3.1. Mass and Magnetic Flux Conservation

Before we address the conservation of energy, however, we must first establish whether the system is acting like a one-dimensional flux tube. We introduce the solid angle subtended by the flux tube at each spacecraft (Ω) and refer to the ratio of this at both spacecraft as the stream's expansion factor f. We expect each stream to conserve mass flux such that

$$\frac{dM}{dt}\Big|_{\substack{\text{Solar}\\\text{Parker}}}^{\text{Orbiter}} = \Omega n_p u_{cm} r^2\Big|_{\substack{\text{Solar}\\\text{Parker}}}^{\text{Orbiter}} = 0. \quad (1)$$

Using the characteristic values in Tables 1 and 2, we compute that mass conservation for the slow solar wind stream occurs for expansion factor

$$f_{slow} = \frac{\Omega_{\text{Solar Orbiter}}}{\Omega_{\text{Parker}}} = \frac{n_p u_{cm} r^2|_{\text{ Parker}}}{n_p u_{cm} r^2|_{\text{ SolarOrbiter}}} = 0.91 \pm 0.13, \quad (2)$$

and for the Alfvénic slow solar wind,

$$f_{\text{Alfvenic}} = \frac{\Omega_{\text{SolarOrbiter}}}{\Omega_{\text{Parker}}} = \frac{n_p u_{cm} r^2|_{\text{ Parker}}}{n_p u_{cm} r^2|_{\text{ SolarOrbiter}}} = 0.72 \pm 0.21 \quad (3)$$

The Ω is the angular wedge traversed across the flux tube in the individual streams. The center-of-mass velocity is

computed as

$$u_{\rm cm} = \frac{\Sigma_j m_j n_j v_j}{\Sigma_j m_j n_j}. \quad (4)$$

Parameter, r, is the heliocentric distance of the spacecraft and n_j, m_j, and v_j for the species, $j \in [p, \alpha]$, that are the protons and alpha particles. Therefore, the tube is approximately conical (f is near unity in each case) but has underexpanded by a factor of up to ∼13% and 28% for the slow and Alfvénic slow cases, respectively. We therefore set the flux tube expansion factor as $f = 0.91$ and 0.72 between the spacecraft. Y. J. Rivera et al. (2024b) find the flux tube expansion factor for the fast solar wind period (blue shaded region in Figure 3) in this encounter to be 0.90 ± 0.09. This is similar to the analysis in a ∼600 km s^{-1} coronal hole stream from S. J. Schwartz & E. Marsch (1983), which finds a value of $f \sim 0.88$ for a Helios 1 and 2 spacecraft lineup (0.2 au separation), suggesting some flux tube compression between 0.5 and 0.72 au, in line with the present study.

To confirm that this underexpansion in terms of mass flux is balanced by a corresponding change in magnetic flux, we also assess conservation of mass and magnetic flux together across our flux tube. Since this environment is confined to a single positive polarity magnetic sector, we do not expect any annihilation, although some reconnection has been reported in the form of jets beyond 0.6 au in slower speed solar wind (N. Fargette et al. 2023). We can check simply by relating the magnetic flux scaling of $B_r \cdot r^2$ to the mass flux $n_p \cdot v_p \cdot r^2$, as $n \cdot v_p / B_r =$ constant. Using the average values of the time frames of interest from Tables 1 and 2, we compute a ratio of 1.10 ± 0.11 and 1.05 ± 0.16, respectively. A near-unity value of this quantity indicates that the magnetic and mass fluxes both indicate the same expansion factor for the stream, and the streams therefore behave as conservative 1D flux tubes between the two spacecraft.

3.2. Conservation of Energy

In order to model the conservation of energy in the solar wind stream, we model it as a persistent, radial flux tube of solid angle Ω. In the observations, the spacecraft traverses across a flux tube ∼2° wide for the slow wind and ∼6° wide for the Alfvénic slow wind. The plasma is sampled at distances centered on approximately $r_{\rm PSP} \sim 13.4\ R_\odot$ and $r_{\rm SolarOrbiter} \sim 124\ R_\odot$ for the slow wind and $r_{\rm PSP} \sim 13.8\ R_\odot$ and $r_{\rm SolarOrbiter} \sim 131\ R_\odot$ for the Alfvénic slow wind. Physical quantities are assumed to be uniform across the cross section of each flux tube and therefore to only vary with heliocentric distance.

In both streams, significant contributions come from the kinetic energy of the plasma bulk flow, $n_j m_j v_j^2/2$, the thermal energy carried by the plasma, $n_j k_{\rm B} T_j$, and gravitational energy, $m_j n_j G M_\odot (1 - R_\odot/r)/R_\odot$, where the species that we consider, $j \in [e, p, \alpha]$, are the protons, electrons, and alpha particles. As the slow and Alfvénic slow wind includes noncompressible Alfvénic fluctuations, we also consider the energy associated with these waves, $\delta B^2/2\mu_0$, carried by the Alfvén waves throughout these periods. We also quantify the associated heat fluxes, which can become nonnegligible in the slowest wind streams (J. S. Halekas et al. 2023).

We can write the conservation of energy flux, W, in the flux tube segment in terms of the center-of-mass frame of these components following the analysis from S. A. Jacques (1977) and Y. J. Rivera et al. (2024b):

$$W|_{\rm Parker}^{\rm Solar\ Orbiter} = u_{\rm cm} r^2/R_\odot^2 \Omega \times \left(\frac{n_j m_j u_{\rm cm}^2}{2} + \frac{5}{2} n_j k_{\rm B} T_j + \frac{m_j n_j G M_\odot}{R_\odot}(1 - R_\odot/r) + (3/2 + V_{\rm A}/u_{\rm cm}) \frac{\delta B^2}{2\mu_0} + E_{Qe} \right) \times |_{\rm Parker}^{\rm Solar\ Orbiter} = 0. \quad (5)$$

Therefore, the system is in a steady state if the change to the energy flux is zero. The first four components include the kinetic, enthalpy, gravitational, and wave energy terms, where the leading term outside the parentheses is a normalizing factor, $r^2/R_\odot$, scaled to a solar radius (M. Liu et al. 2021). We also compute the electron (E_{Qe}) and proton heat fluxes for the two periods at PSP. We assume a polytropic index for an ideal gas with 3 degrees of freedom ($\gamma = 5/3$) to compute the enthalpy term. The contribution of the electron heat flux in the Alfvénic slow wind period is small, being on the order of 0.01 W m^{-2} (or 0.02%), while it is several orders of magnitude larger for the slow wind period, at ∼4%. Therefore, we include the contribution of the electron heat flux, as calculated in J. S. Halekas et al. (2023), in the energy conservation of the slow wind period. However, we note that the electron heat flux was only computed at PSP because of the unavailable electron measurements at Solar Orbiter for this time frame and assumed to contribute the same energy flux percentage at Solar Orbiter, consistent with statistical results from J. S. Halekas et al. (2023). Therefore, the overall relative contribution to the total energy flux is the same at PSP and Solar Orbiter, and that energy is conserved. We calculate the proton heat flux to be ≪1% in each stream and therefore exclude it from the energy flux calculation.

In our equation, n_j, m_j, and T_j are the number density, mass, and temperature, respectively, of the protons, electrons, and alpha particles. B is the magnetic field, and $V_{\rm A}$ is the local Alfvén speed. G, $k_{\rm B}$, $M_\odot$, $R_\odot$, and μ_0 are the gravitational constant, Boltzmann constant, mass and radius of the Sun, and permeability of free space, respectively.

Tables 3 and 4 list the averages for individual energy terms calculated in the center-of-mass frame for the total of the proton, alpha, and electron populations following Equation (5) to determine whether the energy supplied at the base of the flux tube is conserved between the spacecraft. The Solar Orbiter energy fluxes at each stream are multiplied by their individual expansion factors, $f_{\rm slow} = 0.9$ and $f_{\rm Alfvenic} = 0.72$, to appropriately account for their compression. Figure 4 is a visual representation of the contribution of the individual energy flux terms at PSP and Solar Orbiter, multiplied by their compression factors, for the slow wind and Alfvén slow wind. The figures include all the energy terms listed in Tables 3 and 4. As the figure illustrates, and as indicated by the total energy flux in the related tables, energy conservation is met within the standard deviation of the total energy flux for both solar wind streams.

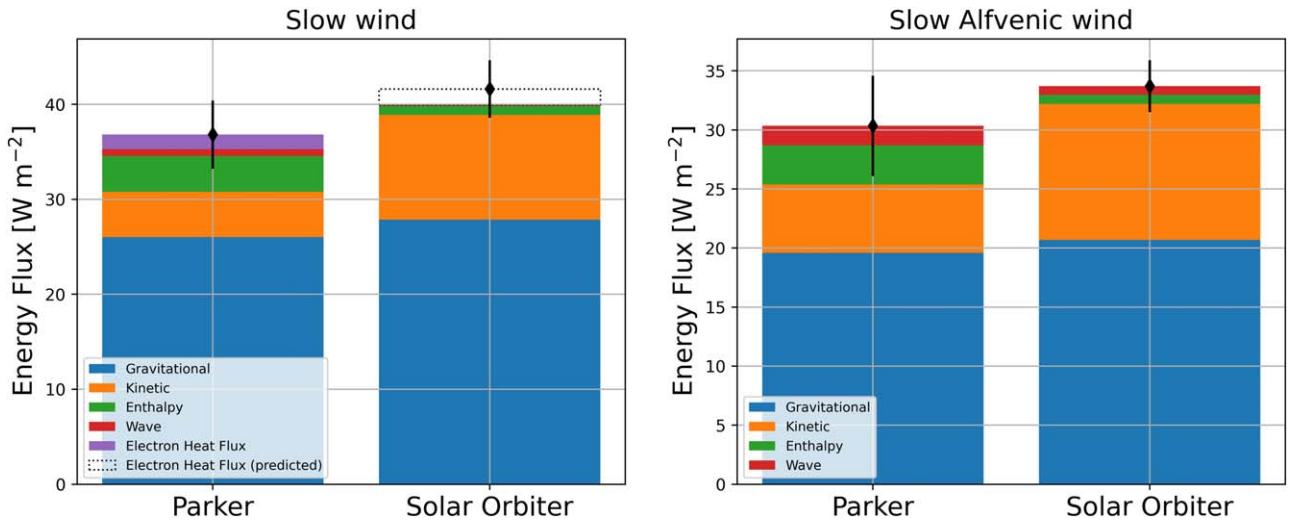

Figure 4. Energy fluxes at PSP and Solar Orbiter for the slow (left) and Alfvénic slow (right) solar wind. The values are computed from Equation (5) and listed in Tables 1 and 2.

Table 3
Individual Energy Terms and Standard Deviation Computed from Equation (5) for PSP and Solar Orbiter Averaged across Source Surface Longitude 116°−118° (as Indicated in Figure 2) and Normalized by the Flow Speed and Solar Radii

Slow Wind: Energy Flux Terms $\times (r/R_\odot)^2$	PSP (W m^{-2})	Solar Orbiter (W m^{-2} $\times f$)	Δ Solar Orbiter − PSP
W_{Kinetic}	4.76 ± 0.68	11.02 ± 0.95	6.26 ± 1.17
W_{Enthalpy}	3.76 ± 0.43	0.93 ± 0.08	−2.83 ± 0.44
$W_{\text{Gravitational}}$	26.03 ± 2.08	27.87 ± 2.01	1.84 ± 2.89
W_{Wave}	0.73 ± 0.58	0.13 ± 0.11	−0.60 ± 0.59
W_{Qe}	1.54 ± 0.51	1.61 ± 0.53[a]	0.07 ± 0.74
Total	36.82 ± 3.60	41.56 ± 3.04	4.74 ± 4.30

Notes. The values of Solar Orbiter are multiplied by a characteristic expansion factor, f_{slow}, computed from mass conservation in Equation (2).
[a] Calculated based on an equal relative energy flux at Solar Orbiter.

Table 4
Individual Energy Terms and Standard Deviation Computed from Equation (5) for PSP and Solar Orbiter Averaged across Source Surface Longitude 140°−146° (as Indicated in Figure 2) and Normalized by the Flow Speed and Solar Radii

Alfvénic Slow Wind Energy: Flux Terms $\times (r/R_\odot)^2$	PSP (W m^{-2})	Solar Orbiter (W m^{-2} $\times f$)	Δ Solar Orbiter − PSP
W_{Kinetic}	5.78 ± 1.53	11.54 ± 2.31	5.76 ± 2.77
W_{Enthalpy}	3.10 ± 0.70	0.76 ± 0.15	−2.34 ± 0.72
$W_{\text{Gravitational}}$	19.59 ± 2.95	20.67 ± 2.80	1.08 ± 4.06
W_{Wave}	1.64 ± 1.1	0.73 ± 0.45	−0.91 ± 1.19
Total	30.34 ± 4.24	33.70 ± 2.20	3.36 ± 4.78

Note. The values of Solar Orbiter are multiplied by a characteristic expansion factor, f_{Alfvenic}, computed from mass conservation in Equation (3).

Under the well-supported hypothesis that these are the same streams, as indicated through the conserved quantities and stream properties discussed, we explore the degree to which dissipation of Alfvén waves in each stream may be the source of sufficient energy to allow for a self-consistent (i.e., mass- and energy-conserving) heating and acceleration.

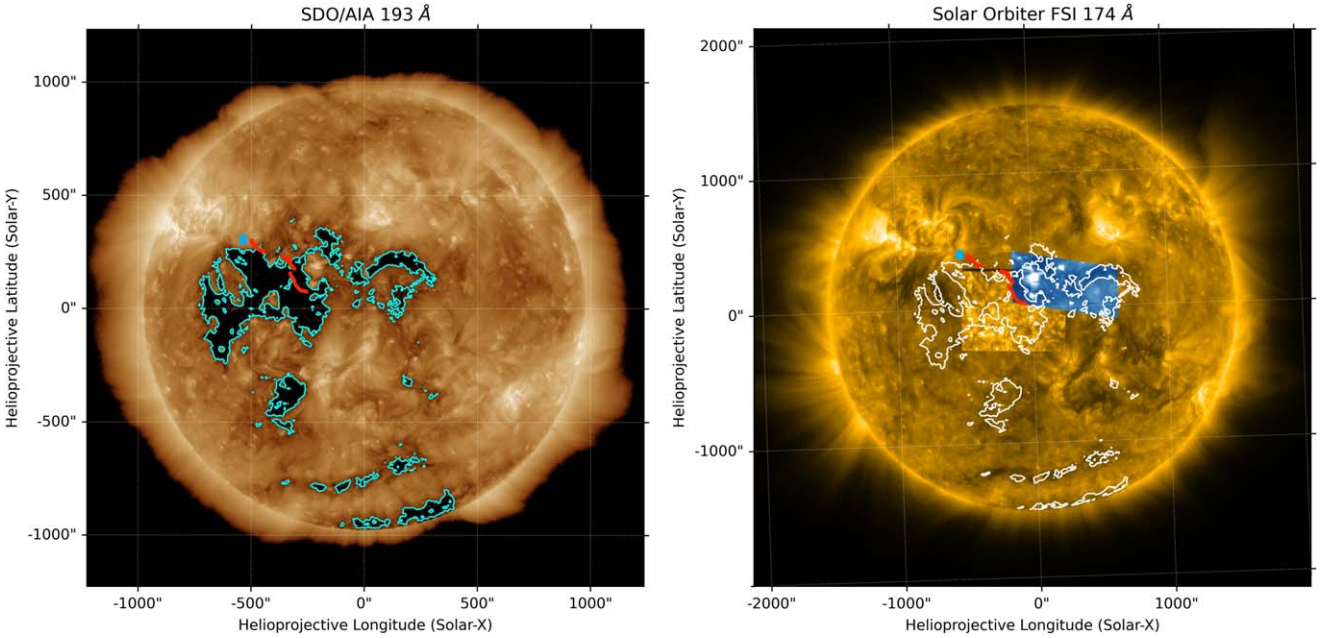

Figure 5. Full-disk images of SDO/AIA 193 Å on 2022 February 23 00:30 UT (left) and Solar Orbiter FSI 174 Å on 2022 February 23 11:21 UT (right). The outline indicates the coronal hole boundary determined by AIA 193 Å and mapped to FSI 174 Å. The FSI contains the SPICE raster of the Ne VIII 770.42 Å taken on 2022 February 23 11:23–10:06 UT and Hinode/EIS raster of the Fe XII 192.813 Å taken on 2022 February 23 00:30–01:31 UT.

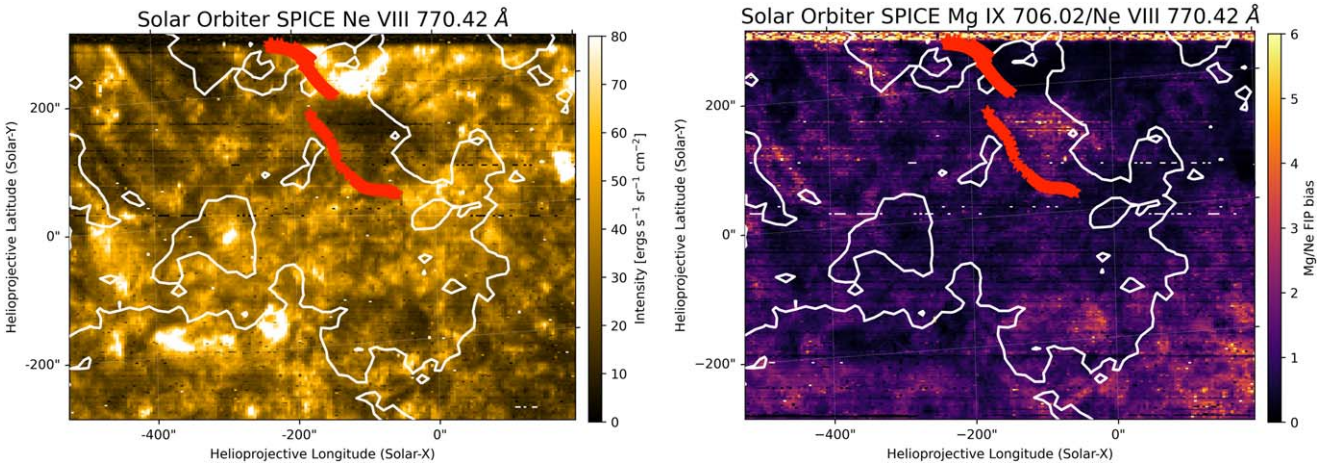

Figure 6. Solar Orbiter SPICE intensity of the Ne VIII 770.42 Å (left) and FIP bias of Mg/Ne (right). The white outline is the coronal hole outline from Figure 5. The red stars show the footpoint mapping for the Alfvénic slow solar wind corresponding to the red time frame in Figure 3.

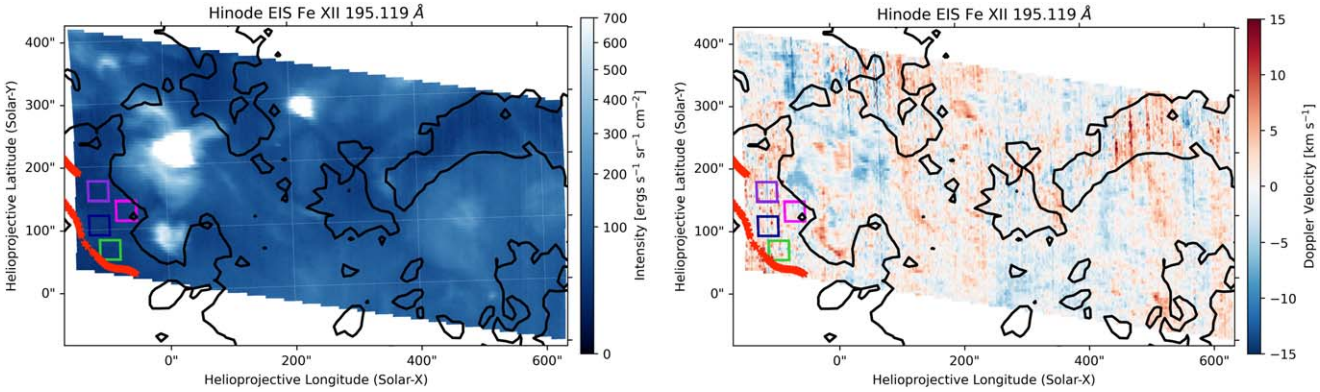

Figure 7. Hinode/EIS observations of the Fe XII 195.119 Å fitted intensity (left) and velocity Doppler shifts (right). The black (left) and white (right) outline is the coronal hole outline from Figure 5.

4. Coronal Properties

4.1. Solar Wind Source Mapping

To explore the coronal properties of the solar wind and explore its conditions below PSP's orbit, we examine several remote observations from Hinode and Solar Orbiter. The backmapped solar wind trajectories at 2.5 $R_\odot$ are subsequently mapped to estimates of the photospheric source locations using potential field source surface modeling of the coronal magnetic field. The resulting footpoints are overlaid on various remote sensing observations in Figures 5, 6, and 7.

Figure 5 shows the Sun from the FOV of SDO/AIA in the 193 Å (left) and Solar Orbiter FSI 174 Å (right) with the associated fast (blue) and Alfvénic slow (red) footpoints. The FSI includes a SPICE Ne VIII 770.42 Å and EIS Fe XII 192.813 Å intensity raster taken the same day. The cyan outline in the AIA 193 Å images indicates the overall boundary of the coronal hole structure determined from an intensity threshold of emission with intensity below 90 DN s^{-1} simply as a reference between the remote observations. The coronal hole outline determined from AIA is mapped directly to the FSI 174 Å image as the white outline, as well as the SPICE and EIS observations discussed below. We note that the footpoints for the slow wind appear to the left of the fast wind footpoints but are not included in the figures. We find that the footpoints associated with the fast and Alfvénic slow wind are associated with the boundary of the extended equatorial coronal hole network. The footpoints for the Alfvénic slow solar wind fall within the SPICE raster and at the lower left of the EIS FOV, which both observe part of the same coronal hole structure nearly contemporaneously. The SPICE observations provide a comparison between the elemental composition at the Sun with those measured with HIS in situ, while the EIS observations provide electron density and temperature constraints in the corona.

4.2. Elemental Composition

We compare the remotely observed and in situ elemental abundances from Solar Orbiter to confirm that the heliospheric to photosphere mapping is reasonable and to justify the coronal constraint in the solar wind modeling from the source conditions, i.e., electron temperature and density from Section 4.3. Figure 6 shows the SPICE raster from Figure 5, showing the intensity (left) and the FIP bias of Mg/Ne (right) with the same coronal hole outline. The Mg/Ne elemental abundance can be used to compare with the elemental abundances (Fe/O) measured in situ with Solar Orbiter, where similarly low-FIP enhanced ratios can be utilized to confirm footpoint connection. The intensity from SPICE is computed by integrating over the fitted Gaussian profile of the Ne and Mg spectral lines. The FIP bias is determined by taking an intensity ratio of Mg IX 706.02 Å (low FIP, 7.6 eV) and Ne VIII 770.42 Å (high FIP, 21.6 eV) following analysis for SPICE observations in D. H. Brooks et al. (2022) and T. Varesano et al. (2024). The intensity governed by collisional excitation, in units of photons cm^{-2} s^{-1} $arcsec^{-2}$, is given as

$$I_{\rm coll} = \frac{1}{4\pi}\int_{-\infty}^{\infty} G(T, n_e)\varphi(T)dT, \tag{6}$$

where T and n_e are the electron temperature and density, respectively. $G(T, n_e)$ is the contribution function in units of cm^3 s^{-1}. $\varphi(T)$ is the differential emission measure (DEM) in units of cm^{-5} K^{-1}. They are defined as follows:

$$G(T, n_e) = \frac{n_j(X^{+q})}{n(X^{+q})}\frac{n(X^{+q})}{n(X)}\frac{n(X)}{n(\mathrm{H})}\frac{n(\mathrm{H})}{n_e}\frac{A_{ji}}{n_e} \tag{7}$$

$$\varphi(T) = n_e^2\frac{dx}{dT}, \tag{8}$$

where $n_j(X^{+q})/n(X^{+q})$ is the population of level j of the $+q$ ion of element X, $n(X^{+q})/n(X)$ is the relative abundance of the $+q$ state, $n(X)/n(H)$ is the absolute abundance, $n(H)/n_e$ is the hydrogen-to-electron ratio, and A_{ij} is the Einstein coefficient for spontaneous emission. The spectral line analysis uses atomic properties and tools from CHIANTI v.10 (G. Del Zanna et al. 2021) using version 0.2.3 (W. Barnes et al. 2024) of the fiasco open-source software package. For the SPICE observations, the spectral lines were chosen because their ions span a similar temperature range; therefore, their ratio is largely independent of temperature. The FIP bias is a ratio of the elemental abundances that can be calculated by separating the elemental abundances from the contribution function, Ab(Mg) $= n(\mathrm{Mg})/n(\mathrm{H})$ to Ab(Ne) $= n(\mathrm{Ne})/n(\mathrm{H})$, and inverting the equation such that

$$\frac{\mathrm{Ab_{Mg}}}{\mathrm{Ab_{Ne}}} = \frac{I_{\rm Mg}}{I_{\rm Ne}}\frac{C(T, n_e)_{\rm Ne}}{C(T, n_e)_{\rm Mg}}, \tag{9}$$

where

$$G(T, n_e) = \mathrm{Ab} \times C(T, n_e). \tag{10}$$

Under ionization equilibrium conditions, the peak of the formation temperature curve for Mg IX is $\log_{10}(T\ [\mathrm{K}]) = 6.0$ and that for Ne VIII is $\log_{10}(T\ [\mathrm{K}]) = 5.8$. Therefore, the emission observed is largely associated with plasma with temperatures spanning the typical transition region and low corona plasma associated with the quiet Sun and coronal holes.

We note that there is a nonnegligible difference in peak formation temperature in the two lines chosen for the abundance analysis. Therefore, changes in the Mg/Ne FIP bias map of Figure 6 may arise simply from changes in temperature given that the lines span a slightly shifted formation temperature range. However, it is generally found that coronal holes have small temperature variation and are observed to be fairly stable, isothermal structures in the corona (M. Hegde & K. M. Hiremath 2024). Statistical coronal hole DEMs indicate a narrow peak at ~1 MK and a much smaller peak at ~1.5 MK that remain consistent across several solar rotations (J. Saqri et al. 2020). However, they may have some small radial variation (E. Landi 2008). The variation in the temperature analysis from EIS in Section 4.3 is also in line with small temperature changes across the coronal hole. Therefore, we do not expect a strong, large-scale spatiotemporal temperature gradient in the coronal hole examined in this study, and we attribute Mg/Ne FIP bias variability in Figure 6 in large part to changes in its compositional properties. Some variation in high-FIP Ne has been observed during solar minimum that have been expressed remotely (E. Landi & P. Testa 2015) and in situ (P. Shearer et al. 2014); however, we do not expect these effects to drive changes in the SPICE observations at solar maximum.

Through this implementation, we find that the FIP bias of low-FIP Mg and high-FIP Ne across the raster falls within 1–6. A large portion of the coronal hole is between 1 and 2, with the

Table 5
List of Average Intensities for Different Spectral Lines of Each Box Shown in Figure 7 That Are Used in the Temperature Calculation in Figure 8

Spectral Line	Intensity			
	Purple	Blue	Green	Magenta
Fe XI 188.216	67	62	66	71
Fe XI 188.299	59	54	59	63
Fe XI 192.813	49	45	49	52
Fe XII 192.394	21	19	22	23
Fe XII 195.119	70	60	65	69
Fe XIII 202.044	82	82	49	58
Fe XIII 203.826	27	13	21	49

Note. Intensities are in units of ergs s^{-1} sr^{-1} cm^{-2}, and spectral lines are in units of Å.

edges extending to higher FIP values. The Alfvénic slow wind footpoints correspond to inside of the coronal hole boundary within 1–2 FIP bias values that would coincide with a low-FIP/high-FIP in situ ratio, Fe/O FIP bias, ∼1 at Solar Orbiter, shown in panel (l) of Figure 3. However, we note that the FIP bias map at the Sun shows a range of photospheric (∼1) and low-FIP enhanced regions within and outside of the coronal hole, making it difficult to confirm footpoints with certainty. We also note that the FIP bias comparison between the remote observations and in situ includes ratios from different elements that may undergo different degrees of the FIP effect; therefore, the connection between Mg/Ne (remote) and Fe/O (in situ) may not be directly comparable (J. M. Laming et al. 2019). Overall, a more rigorous comparison of elemental abundances requires several matching elemental ratios between remote and in situ heavy ions (Y. J. Rivera et al. 2022).

4.3. Electron Temperature and Density

Given that EIS observes lines from more highly ionized ions in the corona, we use those observations to determine a coronal temperature and density associated near the edge of the coronal hole boundary to compare with the isothermal radius modeling discussed in Section 5. Figure 7 shows the EIS intensity (left) and Doppler shift (right) map of the Fe XII 195.119 Å spectral line, with the coronal hole outline overlaid. Using the EIS Python Analysis Code (EISPAC) software package (M. J. Weberg et al. 2024), the intensity is computed by integrating over the fitted Gaussian profile of the Fe XII spectral line. The Doppler shifts are computed as the shift of the fitted line centroid from the theoretical emission-line peak in km s^{-1}. A red Doppler shift shows plasma moving away from the observer, while a blueshift shows plasma moving toward the observer.

We identify four small 20″ × 20″ regions near the edge and inside of the coronal hole, shown as purple, blue, green, and red boxes in Figure 7, which would correspond to the Alfvén slow solar wind footpoints. The plasma is assumed to be uniform in temperature and density within each of the boxes. To determine the electron density, we use the standard density-sensitive line pair, Fe XIII 202.044/203.826, where the intensity ratio simplifies to the ratio of their contribution functions (D. H. Brooks & H. P. Warren 2011; D. H. Brooks et al. 2022). We list the lines and their intensities in Table 5. The average electron densities within purple, blue, green, and magenta boxes are 5.9 × 10^8 cm^{-3}, 1.6 × 10^8 cm^{-3}, 4.6 × 10^8 cm^{-3}, and 9.8 × 10^8 cm^{-3}, respectively. We include these estimates in the solar wind modeling results as a constraint to the proton density in comparison to the initial density, under the assumption that quasi-neutrality holds.

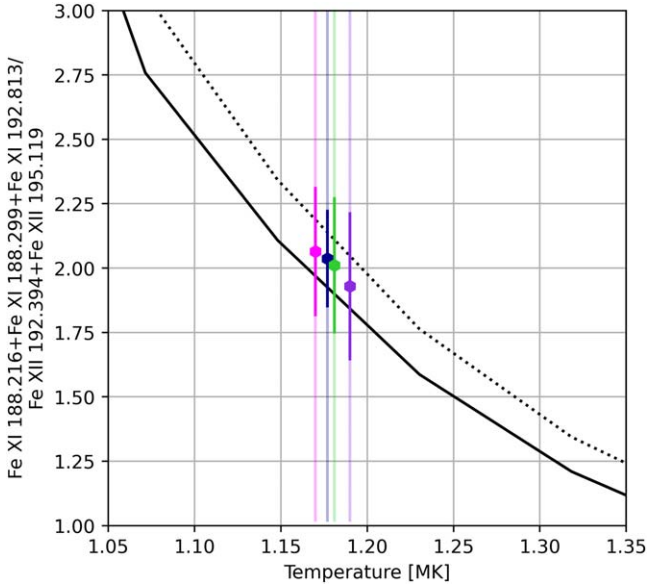

Figure 8. Ratio of the average intensity within each box in Figure 7 for the sum of the Fe XI 188.216 + Fe XI 188.299 + Fe XI 192.813 to the sum of Fe XII 195.119 + Fe XII 192.394 shown for each corresponding color. The theoretical curves of the intensity ratio across electron temperature are in black, as derived using CHIANTI v.10 atomic values for the minimum (solid) and maximum (dashed) electron density computed from the Fe XIII line ratio.

Traditionally, EIS observations provide lines from several consecutive Fe ions to derive a DEM of the observed plasma as a function of temperature. A well-constrained DEM curve can be used to determine an electron temperature. However, the lines observed during the raster in the present study are limited owing to a noisy signal inside the coronal hole boundary. Instead, we estimate the temperature using a line ratio of consecutive ions using a sum of the Fe XI 188.216 + Fe XI 188.299 + Fe XI 192.813 to the sum of Fe XII 195.119 + Fe XII 192.394 to estimate an electron temperature for each box, as listed in Table 5. Figure 8 shows the range of temperatures for each corresponding box, indicating a source temperature of ∼1.17−1.19 MK. We include this temperature estimate in solar wind modeling results as a constraint to the electron temperature.

5. Radial Profiles and Parker Solar Wind Model Comparison

Following Y. J. Rivera et al. (2024b), we implement two-fluid, "iso-poly" Parker solar wind models (J.-B. Dakeyo et al. 2022) and implement an external fitted wave force based on two points of constraint from the Alfvén wave pressure. These measurements are used to constrain an analytic formula (C. Shi et al. 2022), which is essentially a power law between the two measured points and parameterized by an amplitude f_0 in units of $GM_\odot/R_\odot^2$ and a power-law index ν (see Y. J. Rivera et al. 2024b, for more details).

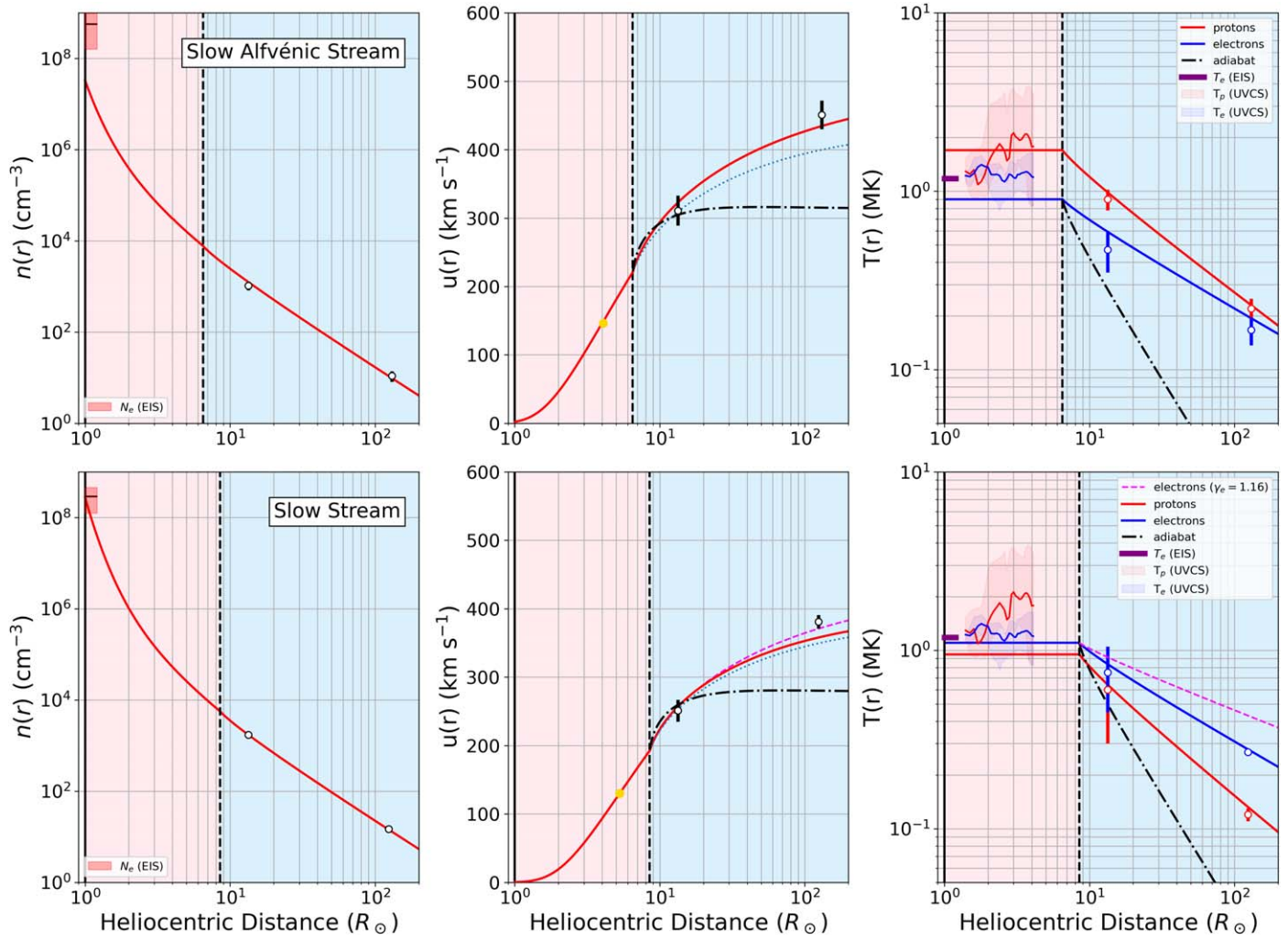

Figure 9. Parker solar wind solutions and associated data constraints for the Alfvénic slow (top row) and slow (bottom row) wind. From left to right: proton density, proton velocity, and proton (red) and electron (blue) temperatures. For the acceleration profiles (middle column), solutions are shown both with (solid) and without (dotted) Alfvénic wave pressure, as well as for the adiabatic/non-Alfvénic wave pressure case (dashed–dotted). For the slow stream (bottom row) an additional solution is shown with the electron polytropic index decreased (made closer to isothermal) to illustrate the magnitude of the change needed to explain the observed acceleration (dashed magenta). The white circles are the average properties at PSP and Solar Orbiter for the slow wind in Table 1 and Alfvénic slow wind in Table 2. We also include remote observations of coronal density and electron temperature derived in Section 4.3 from EIS and the electron and proton temperature from previously examined coronal holes from UVCS observations over the poles during the period of 1996–1997 (S. R. Cranmer 2020).

Table 6
Parameters for the Solar Wind Models Shown in Figure 9

Stream	n_{p0} (cm^{-3})	T_{p0} (MK)	T_{e0} (MK)	γ_p	γ_e	$R_{\rm iso}$ ($R_\odot$)	[f_0 ($GM_\odot/R_\odot^2$), ν]
Slow Alfvénic	3.3×10^7	1.7	0.9	1.3	1.23	6.5	[3.7×10^{-4},1.5]
Slow	2.3×10^8	0.95	1.1	1.33	1.23	8.5	[4.1×10^{-4},1.1]

This modeling approach solves the 1D radial expansion of a hydrodynamic fluid under the joint effects of outward thermal pressure gradients from electrons and protons, the aforementioned wave pressure gradient, and the inward force of gravitation. The results are shown in Figure 9, where the models and data constraints on density, velocity, and temperature (for both protons and electrons) are plotted.

The models couple two distinct thermal regimes: an isothermal corona (E. N. Parker 1958) and a polytropic ($\gamma \langle 5/3$) inner heliosphere (E. N. Parker 1960) in the young solar wind. Varied parameters are the average isotropic temperatures of the protons and electrons in the corona, the polytropic index of both protons (γ_p) and electrons (γ_e), and the radius at which the thermal regime transitions from corona to inner heliosphere ($R_{\rm iso}$). These parameters set the temperature profiles (right column of Figure 9), and the acceleration profiles are then prescribed (middle column of Figure 9). The density curve follows mass flux conservation (left column of Figure 9) and is matched to measurements by varying a reference density (n_{0p}) at 1 $R_\odot$.

Measured proton temperatures at both spacecraft provide a strong constraint on the proton polytropic index, γ_p. For the

electron temperatures we obtain measurements at PSP from J. S. Halekas et al. (2020), while in lieu of a Solar Orbiter measurement we use the statistically derived electron polytropic index most appropriate for the observed wind speeds from J.-B. Dakeyo et al. (2022). The temperature constraints also couple $R_{\rm iso}$ and the coronal temperatures (T_{p0},T_{e0}): since the derived temperature profiles are fitted to the observations in the interplanetary medium, decreasing $R_{\rm iso}$ increases the necessary coronal temperature. These three parameters are therefore varied together to find a solution that best matches the observed acceleration of the stream while remaining consistent with coronal constraints.

The end results are the modeling parameters recorded in Table 6. In Figure 9, we plot the resulting solutions both with (dotted lines) and without (solid lines) the effect of the observed wave energy flux, as well as the solutions for the adiabatic case (dashed–dotted lines). We also include coronal proton and electron measurements determined remotely from the UltraViolet Coronagraph Spectrometer (UVCS) computed in S. R. Cranmer (2020) and from the analysis of EIS observations in Section 4.3 to compare with the resulting isothermal layer extrapolations. The UVCS temperatures were computed for polar coronal holes between 1996 and 1997 and most representative of fast wind conditions. For comparison to the modeled density profile, we include the computed electron density (from EIS) as the proton density at the solar surface.

For the Alfvénic slow wind stream (top row), the observed thermal pressure gradients (within the temperature measurement error bars) and wave energy flux can explain the observed acceleration. Moreover, the wave energy flux is seen to be important for this stream, similar to that reported in Y. J. Rivera et al. (2024b) for fast wind. Without it the accelerated stream only reaches 400 km s^{-1} at Solar Orbiter, but with it the observed speed reaches within error bars of the 451 ± 21 km s^{-1} measurement. In the adiabat case, the acceleration beyond PSP is negligible. We note that even with both the thermal and wave pressures (and the thermal pressure near the top of the measurement error bars) the achieved acceleration is still slightly below the mean measurement. This may indicate that other contributions, for example, the effect of stream interactions, are needed to fully account for the stream evolution.

Meanwhile for the slow stream (bottom row), the effect of wave energy flux is negligible (see J. S. Halekas et al. 2022, 2023). However, no combination of parameters that matched the temperature observations was found to fully explain the observed acceleration. Decreasing the electron polytropic index by 6% of the statistical value from J.-B. Dakeyo et al. (2022) for a $\gamma_e = 1.16$ quantifies the additional pressure needed to solve the gap (magenta dashed curves), but other processes such as transverse density gradients or non-Alfvénic wave pressure may play a role given that Alfvénic wave pressure cannot explain this gap.

We also note that while proton thermal pressure dominates over electron thermal pressure in the slow Alfvénic case, the inverse is true for the slow wind case in our study. In all regards, the Alfvénic slow wind stream here qualitatively resembles the properties of fast wind, consistent with many prior studies (R. D'Amicis & R. Bruno 2015; R. D'Amicis et al. 2019, 2021; T. Ervin et al. 2024b).

6. Discussion

The work maps a single stream of slow and Alfvénic solar wind from the Sun to the inner heliosphere to trace large-scale energetics within their radial evolution. Both streams are intercepted by PSP ($\sim$13 $R_\odot$) and Solar Orbiter ($\sim$130 $R_\odot$), where the streams are matched by comparing magnetic field polarity, compositional properties, and conserved quantities based on their ballistically backmapped source surface footpoints. Mass, magnetic, and total energy flux (kinetic, enthalpy, gravitational, wave) is conserved between their heliocentric locations within the variability of the stream properties. Energy flux conservation suggests that the energy within each stream is exchanged self-consistently across the components.

Through a comparison of the energy flux budgets of the slow and Alfvénic slow wind, we find that different energy components drive their respective heating and acceleration through the inner heliosphere. The Alfvénic slow solar wind contains a larger relative wave energy flux contribution to the total energy flux ($\sim$7%) compared to the non-Alfvénic slow wind ($\sim$2%) at PSP. The wave energy flux is found to decay to $\sim$2.3% (Alfvénic) and $\sim$0.4% (non-Alfvénic) of the total energy flux by Solar Orbiter. In comparison, a fast wind stream from a similar period and heliocentric evolution (from the blue shaded region in Figure 3) is found to contain a larger relative wave energy flux contribution of $\sim$10% that decreases to $\sim$1% of the total energy budget between PSP and Solar Orbiter (Y. J. Rivera et al. 2024b). In the case of the enthalpy contribution at PSP, the slow wind stream is dominated by the electron population, where $T_e/T_p = 1.25$, while this ratio is only about 0.5 in the Alfvénic slow wind. In comparison to the fast wind case, the temperature ratio at PSP is found to be smaller than both slow wind cases, $T_e/T_p = 0.35$ (Y. J. Rivera et al. 2024b). In both the slow wind cases, the decrease in the enthalpy and wave energy flux is balanced by an increase in the kinetic and gravitational terms, such that energy is conserved, as visualized in Figure 4. We note that the electron heat flux has a larger relative contribution at PSP in the slow versus Alfvénic slow wind stream, and therefore it is included in the energy budget. However, the unavailable electron measurements at Solar Orbiter inhibited a direct computation of the electron heat flux there. Instead, we use the same $\sim$4% contribution as was found at PSP distances, in accordance with statistical results from J. S. Halekas et al. (2023). Therefore, the electron heat flux in the slow wind stream is expected to remain at 4%.

Overall, the two-fluid, iso-poly + wave forcing Parker solar wind modeling results show that the observed wave energy flux and associated wave pressure gradient are necessary components to explain the full Alfvénic slow wind acceleration, in addition to the nonadiabatic proton thermal pressure gradient. In contrast, the slow wind's acceleration is largely accounted for by the nonadiabatic thermal pressure gradient of the electrons, with a smaller proton contribution, without a significant contribution from the wave pressure gradient. We note that while the waves are not contributing to the direct acceleration of the solar wind in this stream, their dissipation may still be relevant to producing the nonadiabatic pressure gradient, which can be driven by ion–cyclotron waves and turbulent dissipation in streams around the HCS (D. Telloni et al. 2023b). A summary of the results for the different cases of the velocity profile is shown in the middle panel of Figure 9. Both the slow and Alfvénic slow wind proton temperature profiles have a similar nonadiabatic cooling profile, with a fitted polytropic index of 1.3 (Alfvénic) and 1.33 (non-

Alfvénic). We find that the two slow wind cases exhibit a shallower proton temperature profile compared to the fast wind case of Y. J. Rivera et al. (2024b), showing $\gamma_p = 1.4$. Because of the missing electron temperature at Solar Orbiter, we instead employ an electron polytropic index, γ_e, from the associated wind speed family of J.-B. Dakeyo et al. (2022). However, we note that the electron temperature profile (blue curve in Figure 9) is not able to fully meet the acceleration exhibited by the stream. We explore the excess forcing needed to resolve this discrepancy. We find that by making the electron temperature curve 6% shallower (smaller polytropic index) than statistical trends, the observed acceleration can be achieved (magenta dashed curve). This entails adding $2\,\mathrm{W\,m^{-2}}$ (roughly 4% of the total energy flux) to the energy budget. It is interesting to note that this is comparable to the $1.75\,\mathrm{W\,m^{-2}}$ present in the electron heat flux at PSP; therefore, if a substantial portion of this was transferred to the protons during transport, it could contribute to this necessary extra forcing while keeping the electron polytropic index more in line with expectations.

Finally, we find that the extrapolated temperature and density simulated curves in the corona are somewhat compatible with remote sensing constraints of the Alfvénic solar wind source region while highly compatible with the slow wind solutions. The solar wind modeling is further constrained through remote observations from Hinode/EIS, where the electron temperature and density were derived for the coronal hole structure associated with the Alfvénic slow solar wind. We also include proton and electron temperature (spanning $1.5-4\ R_\odot$) from a polar coronal hole from S. R. Cranmer (2020) to compare with our temperature results. Given that the PSP iso-poly solar wind solutions are derived completely independently from any coronal observations, their relative agreement lends validity to the resulting stream profile in the isothermal layer. However, the discrepancy observed is likely due to the complexity of the corona itself and the fact that EIS only provides a single height of coronal observations along the LOS. Alternatively, the simulated isothermal temperature region uses the same radius for both proton and electron temperature profiles, which are likely independent. Adjusting the isothermal radius separately could lead to different isothermal temperature results that may be more consistent with the heliospheric electron profile (J.-B. Dakeyo et al. 2022). In addition, we find that the UVCS coronal observations from polar coronal holes are most compatible with the Alfvénic slow solar wind coronal observations from EIS in line with a coronal hole source region, as shown in Figure 5.

Ideally, an off-limb, radial profile (as in the UVCS case) of the proton and electron temperature and density, along with the bulk solar wind speed, including plasma composition, with magnetic field and Alfvén wave properties along the individual streams, would provide more rigorous constraints to plasma source region footpoints and evolution below PSP's orbit. This would only be possible in cases where remote observations (including polarimetric observations that inform on the magnetic field morphology; e.g., T. A. Schad et al. 2024; Z. Yang et al. 2024) of the corona are taken in quadrature with in situ observations of the connected source region footpoints. Future work will examine such a spacecraft alignment to capture more of the extended coronal properties to constrain solar wind energetics across the middle corona (G. Del Zanna et al. 2018; M. J. West et al. 2023).

7. Summary and Conclusions

Through linked remote and in situ observations of a slow and Alfvénic slow solar wind stream, we follow their propagation from the corona through the inner heliosphere. A two-fluid (protons and electrons) implementation of the Parker solar wind solutions with an added wave forcing term, constrained to observations at two heliocentric distances and previous statistical studies, generates the appropriate thermal and wave pressure gradients that explain the observed heating and acceleration of the Alfvénic slow solar wind stream. In contrast, the solutions for the slow solar wind acceleration are generated by the electron and proton thermal pressure gradients, without a significant contribution from Alfvén waves. However, we note that the slow wind requires a slightly shallower electron polytropic index compared to a statistically derived value from a similar asymptotic wind speed profile (using 94% of the stated value from J.-B. Dakeyo et al. 2022 from solar wind family C) to reach the observed speed at Solar Orbiter.

A comparison between the slow, the Alfvénic slow, and a previously studied fast wind stream (Y. J. Rivera et al. 2024b), from the same period, indicates an increasing contribution of the wave energy flux to the energy budget, which is in line with statistical work from J. S. Halekas et al. (2023). The increasing wave energy flux is directly correlated to wind speed, indicating a growing importance of the acceleration of the solar wind. The details of how the waves are converted to heat warrant further investigation; they are likely to involve reflection-driven turbulence (e.g., B. D. G. Chandran & J. V. Hollweg 2009; A. A. van Ballegooijen & M. Asgari-Targhi 2016) and turbulent dissipation (e.g., L. Sorriso-Valvo et al. 2007; B. T. MacBride et al. 2008; J. E. Stawarz et al. 2009). Previous work has shown that turbulent cascade rates (i.e., the rate at which turbulent dynamics bring energy to the small scales to facilitate dissipation) are consistent with the heating rates needed to produce the radial temperature profiles observed in the solar wind. This likely has a direct relationship to the decay of switchbacks discussed in this study (R. Marino et al. 2008; J. E. Stawarz et al. 2009; J. T. Coburn et al. 2012; R. Bandyopadhyay et al. 2023; S. Bourouaine et al. 2024).

Coronal constraints of temperature and density are somewhat compatible with those derived independently with the modeling, but more extended observations of the corona are required to fully constrain the solar wind evolution below PSP's orbit. Previous work has shown great progress in accessing the solar and solar wind connection using remote observations, magnetohydrodynamic (MHD) simulations, and in situ measurements from orbiting spacecraft (S. Parenti et al. 2021; K. J. Knizhnik et al. 2024), with many implementing several points of constraint across the Sun–heliospheric system to connect coronal outflows to the inner heliosphere (D. H. Brooks et al. 2021; D. Telloni et al. 2021; L. Adhikari et al. 2022; D. Baker et al. 2023). Future work will leverage coordinated remote and in situ observations to tracing energetics from deep in the corona to the solar wind.

Acknowledgments

Y.J.R. is partially supported by the Parker Solar Probe project through the SAO/SWEAP subcontract 975569. J.E.S. is supported by the Royal Society University Research Fellowship URF/R1/201286. B.L.A. acknowledges NASA

contract and NASA grants 80NSSC22K0645 (LWS/TM), 80NSSC22K1011 (LWS), and 80NSSC20K1844. K.K.R is funded by the NASA HSO Connect program, grant No. 80NSSC20K1283. Special thanks to Peter Young and Teodora Mihailescu for thoughtful discussion on the Hinode/EIS observations.

Parker Solar Probe was designed, was built, and is now operated by the Johns Hopkins Applied Physics Laboratory as part of NASA's Living with a Star (LWS) program (contract NNN06AA01C). Support from the LWS management and technical team has played a critical role in the success of the Parker Solar Probe mission. Solar Orbiter is a mission of international cooperation between ESA and NASA, operated by ESA. Solar Orbiter SWA data were derived from scientific sensors that were designed and created and are operated under funding provided by numerous contracts from UKSA, STFC, the Italian Space Agency, CNES, the French National Center for Scientific Research, the Czech contribution to the ESA PRODEX program, and NASA. The SWA-HIS team acknowledges NASA contract NNG10EK25C. Solar Orbiter SWA work at the UCL/Mullard Space Science Laboratory is currently funded by STFC (grant Nos. ST/W001004/1 and ST/X/002152/1). The SWA team at INAF/IAPS is currently funded under ASI grant 2018-30-HH.1-2022. Hinode is a Japanese mission developed and launched by ISAS/JAXA, with NAOJ as domestic partner and NASA and STFC (UK) as international partners. It is operated by these agencies in cooperation with ESA and NSC (Norway).

ORCID iDs

Yeimy J. Rivera https://orcid.org/0000-0002-8748-2123
Samuel T. Badman https://orcid.org/0000-0002-6145-436X
J. L. Verniero https://orcid.org/0000-0003-1138-652X
Michael L. Stevens https://orcid.org/0000-0002-7728-0085
Julia E. Stawarz https://orcid.org/0000-0002-5702-5802
Katharine K. Reeves https://orcid.org/0000-0002-6903-6832
Jim M. Raines https://orcid.org/0000-0001-5956-9523
John C. Raymond https://orcid.org/0000-0002-7868-1622
Christopher J. Owen https://orcid.org/0000-0002-5982-4667
Stefano A. Livi https://orcid.org/0000-0002-4149-7311
Susan T. Lepri https://orcid.org/0000-0003-1611-227X
Enrico Landi https://orcid.org/0000-0002-9325-9884
Jasper. S. Halekas https://orcid.org/0000-0001-5258-6128
Tamar Ervin https://orcid.org/0000-0002-8475-8606
Ryan M. Dewey https://orcid.org/0000-0003-4437-0698
Rossana De Marco https://orcid.org/0000-0002-7426-7379
Raffaella D'Amicis https://orcid.org/0000-0003-2647-117X
Jean-Baptiste Dakeyo https://orcid.org/0000-0002-1628-0276
Stuart D. Bale https://orcid.org/0000-0002-1989-3596
B. L. Alterman https://orcid.org/0000-0001-6673-3432

References

Abbo, L., Ofman, L., Antiochos, S. K., et al. 2016, SSRv, 201, 55
Adhikari, L., Zank, G. P., Telloni, D., & Zhao, L. L. 2022, ApJL, 937, L29
Adhikari, L., Zank, G. P., Zhao, L. L., Nakanotani, M., & Tasnim, S. 2021, A&A, 650, A16
Aellig, M. R., Lazarus, A. J., & Steinberg, J. T. 2001, GeoRL, 28, 2767
Alterman, B. L., & Kasper, J. C. 2019, ApJL, 879, L6
Alterman, B. L., Kasper, J. C., Leamon, R. J., & McIntosh, S. W. 2021, SoPh, 296, 67
Asplund, M., Amarsi, A. M., & Grevesse, N. 2021, A&A, 653, A141
Badman, S. T., Bale, S. D., Martìnez Oliveros, J. C., et al. 2020, ApJS, 246, 23
Baker, D., Démoulin, P., Yardley, S. L., et al. 2023, ApJ, 950, 65
Bale, S. D., Badman, S. T., Bonnell, J. W., et al. 2019, Natur, 576, 237
Bale, S. D., Goetz, K., Harvey, P. R., et al. 2016, SSRv, 204, 49
Bale, S. D., Horbury, T. S., Velli, M., et al. 2021, ApJ, 923, 174
Bandyopadhyay, R., Meyer, C. M., Matthaeus, W. H., et al. 2023, ApJL, 955, L28
Barnes, A., & Hollweg, J. V. 1974, JGR, 79, 2302
Barnes, W., Stansby, D., Murphy, N., et al. 2024, tbarnes/fiasco: v0.2.3, Zenodo, doi:10.5281/zenodo.10612118
Belcher, J. W., & Davis, L. J. 1971, JGR, 76, 3534
Bourouaine, S., Perez, J. C., Chandran, B. D. G., et al. 2024, ApJL, 967, L19
Brooks, D. H., Harra, L., Bale, S. D., et al. 2021, ApJ, 917, 25
Brooks, D. H., Janvier, M., Baker, D., et al. 2022, ApJ, 940, 66
Brooks, D. H., & Warren, H. P. 2011, ApJL, 727, L13
Bruno, R., & Carbone, V. 2013, LRSP, 10, 2
Chandran, B. D. G., & Hollweg, J. V. 2009, ApJ, 707, 1659
Coburn, J. T., Smith, C. W., Vasquez, B. J., Stawarz, J. E., & Forman, M. A. 2012, ApJ, 754, 93
Cranmer, S. R. 2020, ApJ, 900, 105
Culhane, J. L., Harra, L. K., James, A. M., et al. 2007, SoPh, 243, 19
Dakeyo, J. B., Badman, S. T., Rouillard, A. P., et al. 2024, A&A, 686, A12
Dakeyo, J.-B., Maksimovic, M., Démoulin, P., Halekas, J., & Stevens, M. L. 2022, ApJ, 940, 130
D'Amicis, R., Alielden, K., Perrone, D., et al. 2021, A&A, 654, A111
D'Amicis, R., & Bruno, R. 2015, ApJ, 805, 84
D'Amicis, R., Matteini, L., & Bruno, R. 2019, MNRAS, 483, 4665
Del Zanna, G., Dere, K. P., Young, P. R., & Landi, E. 2021, ApJ, 909, 38
Del Zanna, G., Raymond, J., Andretta, V., Telloni, D., & Golub, L. 2018, ApJ, 865, 132
De Marco, R., Bruno, R., Jagarlamudi, V. K., et al. 2023, A&A, 669, A108
Ervin, T., Bale, S. D., Badman, S. T., et al. 2024a, ApJ, 969, 83
Ervin, T., Jaffarove, K., Badman, S. T., et al. 2024b, ApJ, 975, 156
Fargette, N., Lavraud, B., Rouillard, A. P., et al. 2021, ApJ, 919, 96
Fargette, N., Lavraud, B., Rouillard, A. P., et al. 2023, A&A, 674, A98
Fox, N. J., Velli, M. C., Bale, S. D., et al. 2016, SSRv, 204, 7
González, C. A., Tenerani, A., Matteini, L., Hellinger, P., & Velli, M. 2021, ApJL, 914, L36
Halekas, J. S., Bale, S. D., Berthomier, M., et al. 2023, ApJ, 952, 26
Halekas, J. S., Whittlesey, P., Larson, D. E., et al. 2020, ApJS, 246, 22
Halekas, J. S., Whittlesey, P., Larson, D. E., et al. 2022, ApJ, 936, 53
Hegde, M., & Hiremath, K. M. 2024, A&A, 688, A35
Horbury, T. S., O'Brien, H., Carrasco Blazquez, I., et al. 2020, A&A, 642, A9
Jacques, S. A. 1977, ApJ, 215, 942
Jagarlamudi, V. K., Raouafi, N. E., Bourouaine, S., et al. 2023, ApJL, 950, L7
Kasper, J. C., Bale, S. D., Belcher, J. W., et al. 2019, Natur, 576, 228
Kasper, J. C., Stevens, M. L., Korreck, K. E., et al. 2012, ApJ, 745, 162
Kasper, J. C., Stevens, M. L., Lazarus, A. J., Steinberg, J. T., & Ogilvie, K. W. 2007, ApJ, 660, 901
Knizhnik, K. J., Weberg, M. J., Provornikova, E., et al. 2024, ApJ, 964, 188
Koukras, A., Dolla, L., & Keppens, R. 2022, arXiv:2212.11553
Laming, J. M., Vourlidas, A., Korendyke, C., et al. 2019, ApJ, 879, 124
Landi, E. 2008, ApJ, 685, 1270
Landi, E., & Testa, P. 2015, ApJ, 800, 110
Lemen, J. R., Title, A. M., Akin, D. J., et al. 2012, SoPh, 275, 17
Lepri, S. T., Landi, E., & Zurbuchen, T. H. 2013, ApJ, 768, 94
Liu, M., Issautier, K., Meyer-Vernet, N., et al. 2021, A&A, 650, A14
Liu, Y. D., Ran, H., Hu, H., & Bale, S. D. 2023, ApJ, 944, 116
Livi, R., Larson, D. E., Kasper, J. C., et al. 2022, ApJ, 938, 138
Livi, S., Lepri, S. T., Raines, J. M., et al. 2023, A&A, 676, A36
Lynch, B. J., Viall, N. M., Higginson, A. K., et al. 2023, ApJ, 949, 14
MacBride, B. T., Smith, C. W., & Forman, M. A. 2008, ApJ, 679, 1644
Macneil, A. R., Owens, M. J., Finley, A. J., & Matt, S. P. 2022, MNRAS, 509, 2390
Marino, R., Sorriso-Valvo, L., Carbone, V., et al. 2008, ApJL, 677, L71
Matthaeus, W. H., & Goldstein, M. L. 1982, JGR, 87, 6011
Nolte, J. T., & Roelof, E. C. 1973, SoPh, 33, 241
Ogilvie, K. W., & Hirshberg, J. 1974, JGR, 79, 4595
Owen, C. J., Bruno, R., Livi, S., et al. 2020, A&A, 642, A16
Parenti, S., Chifu, I., Del Zanna, G., et al. 2021, SSRv, 217, 78
Parker, E. N. 1958, ApJ, 128, 664
Parker, E. N. 1960, ApJ, 132, 821
Perri, S., & Balogh, A. 2010, GeoRL, 37, L17102

Perrone, D., D'Amicis, R., De Marco, R., et al. 2020, A&A, 633, A166
Perrone, D., Perri, S., Bruno, R., et al. 2022, A&A, 668, A189
Phan, T. D., Verniero, J. L., Larson, D., et al. 2022, GeoRL, 49, e96986
Rivera, Y. J., Badman, S. T., Stevens, M. L., et al. 2024a, ApJ, 974, 198
Rivera, Y. J., Badman, S. T., Stevens, M. L., et al. 2024b, Sci, 385, 962
Rivera, Y. J., Higginson, A., Lepri, S. T., et al. 2022, FrASS, 9, 417
Roberts, D. A., Klein, L. W., Goldstein, M. L., & Matthaeus, W. H. 1987, JGR, 92, 11021
Rochus, P., Auchère, F., Berghmans, D., et al. 2020, A&A, 642, A8
Saqri, J., Veronig, A. M., Heinemann, S. G., et al. 2020, SoPh, 295, 6
Schad, T. A., Petrie, G. J., Kuhn, J. R., et al. 2024, SciA, 10, eadq1604
Schwartz, S. J., & Marsch, E. 1983, JGR, 88, 9919
Shearer, P., von Steiger, R., Raines, J. M., et al. 2014, ApJ, 789, 60
Shi, C., Velli, M., Bale, S. D., et al. 2022, PhPl, 29, 122901
Sioulas, N., Shi, C., Huang, Z., & Velli, M. 2022, ApJL, 935, L29
Sorriso-Valvo, L., Marino, R., Carbone, V., et al. 2007, PhRvL, 99, 115001
SPICE Consortium, Anderson, M., Appourchaux, T., et al. 2020, A&A, 642, A14
Stakhiv, M., Landi, E., Lepri, S. T., Oran, R., & Zurbuchen, T. H. 2015, ApJ, 801, 100
Stansby, D., Horbury, T. S., Wallace, S., & Arge, C. N. 2019, RNAAS, 3, 57
Stawarz, J. E., Smith, C. W., Vasquez, B. J., Forman, M. A., & MacBride, B. T. 2009, ApJ, 697, 1119
Stone, E. C., Frandsen, A. M., Mewaldt, R. A., et al. 1998, SSRv, 86, 1
Telloni, D., Andretta, V., Antonucci, E., et al. 2021, ApJL, 920, L14
Telloni, D., Romoli, M., Velli, M., et al. 2023a, ApJ, 954, 108
Telloni, D., Zank, G. P., Adhikari, L., et al. 2023b, ApJ, 944, 227
Tenerani, A., Sioulas, N., Matteini, L., et al. 2021, ApJL, 919, L31
Tu, C. Y., & Marsch, E. 1995, SSRv, 73, 1
van Ballegooijen, A. A., & Asgari-Targhi, M. 2016, ApJ, 821, 106
Varesano, T., Hassler, D. M., Zambrana Prado, N., et al. 2024, A&A, 685, A146
Velli, M., Harra, L. K., Vourlidas, A., et al. 2020, A&A, 642, A4
Wang, Y. M. 2016, ApJ, 833, 121
Weberg, M. J., Warren, H. P., Crump, N., & Barnes, W. 2024, EISPAC—The EIS Python Analysis Code, Zenodo, doi:10.5281/zenodo.12728562
West, M. J., Seaton, D. B., Wexler, D. B., et al. 2023, SoPh, 298, 78
Whittlesey, P. L., Larson, D. E., Kasper, J. C., et al. 2020, ApJS, 246, 74
Xu, F., & Borovsky, J. E. 2015, JGRA, 120, 70
Yang, Z., Tian, H., Tomczyk, S., et al. 2024, Sci, 386, 76